


 CrossMark  
click for updates

 Cite this: *Phys. Chem. Chem. Phys.*,  
2015, 17, 1790

# The importance of inversion disorder in the visible light induced persistent luminescence in Cr<sup>3+</sup> doped AB<sub>2</sub>O<sub>4</sub> (A = Zn or Mg and B = Ga or Al)†

 Neelima Basavaraju,<sup>a</sup> Kaustubh R. Priolkar,<sup>\*a</sup> Didier Gourier,<sup>b</sup> Suchinder K. Sharma,<sup>b</sup> Aurélie Bessière<sup>b</sup> and Bruno Viana<sup>b</sup>

Cr<sup>3+</sup> doped spinel compounds AB<sub>2</sub>O<sub>4</sub> with A = Zn, Mg and B = Ga, Al exhibit a long, near infrared persistent luminescence when excited with UV or X-rays. In addition, the persistent luminescence of ZnGa<sub>2</sub>O<sub>4</sub>, and to a lesser extent MgGa<sub>2</sub>O<sub>4</sub>, can also be induced by visible light excitation via <sup>4</sup>A<sub>2</sub> → <sup>4</sup>T<sub>2</sub> transition of Cr<sup>3+</sup>, which makes these compounds suitable as biomarkers for *in vivo* optical imaging of small animals. We correlate this peculiar optical property with the presence of antisite defects, which are present in ZnGa<sub>2</sub>O<sub>4</sub> and MgGa<sub>2</sub>O<sub>4</sub>. By using X-ray absorption fine structure (XAFS) spectroscopy, associated with electron paramagnetic resonance (EPR) and optical emission spectroscopy, it is shown that an increase in antisite defects concentration results in a decrease in the Cr–O bond length and the octahedral crystal field energy. A part of the defects occurs in the close environment of Cr<sup>3+</sup> ions, as shown by the increasing strain broadening of EPR and XAFS peaks observed upon increasing antisite disorder. It appears that ZnAl<sub>2</sub>O<sub>4</sub>, which exhibits the largest crystal field splitting of Cr<sup>3+</sup> and the smallest antisite disorder, does not show considerable persistent luminescence upon visible light excitation as compared to ZnGa<sub>2</sub>O<sub>4</sub> and MgGa<sub>2</sub>O<sub>4</sub>. These results highlight the importance of Cr<sup>3+</sup> ions with neighboring antisite defects in the mechanism of persistent luminescence exhibited by Cr<sup>3+</sup> doped AB<sub>2</sub>O<sub>4</sub> spinel compounds.

 Received 28th August 2014,  
Accepted 24th November 2014

DOI: 10.1039/c4cp03866e

[www.rsc.org/pccp](http://www.rsc.org/pccp)

## 1 Introduction

Absorption of incident radiation (visible, UV or higher energy) by materials, and delayed subsequent emission most often in the visible range, is termed as long-lasting phosphorescence (LLP) or persistent luminescence. This phenomenon is caused by the trapping of charges (electrons and/or holes) by defects present in the material, preventing fast recombination of the charges. Detrapping of these charges most often proceeds *via* thermal activation giving rise to a progressive radiative recombination prolonging the emission up to several hours.<sup>1</sup> These materials known as persistent phosphors, were demonstrated to be used as probes for *in vivo* small animal optical imaging in 2007, when emitting in the red or near infrared (NIR) range.<sup>2</sup> This technique is advantageous over conventional fluorescence techniques as it avoids autofluorescence of body tissues under continuous illumination and thus improves the signal to noise ratio.

The technique of *in vivo* imaging was first demonstrated using silicate nanoparticles with composition Ca<sub>0.2</sub>Zn<sub>0.9</sub>Mg<sub>0.9</sub>-Si<sub>2</sub>O<sub>6</sub>:Eu<sup>2+</sup>, Dy<sup>3+</sup>, Mn<sup>2+</sup> (CZMSO), with 2.5 mol% of Mn<sup>2+</sup> luminescent ion doping.<sup>2</sup> A new compound, Cr<sup>3+</sup> doped ZnGa<sub>2</sub>O<sub>4</sub>, was reported by Bessière *et al.* in 2011 to be a potential candidate for this imaging application, with enhanced LLP properties.<sup>3</sup> It was demonstrated there that LLP results from Cr<sup>3+</sup> distorted by a neighboring antisite defect, which is the defect resulting from a zinc ion exchanging the site position with a Ga ion or *vice versa*.<sup>3</sup> Soon after that, 0.25 mol% of a Cr<sup>3+</sup> doped ZnGa<sub>2</sub>O<sub>4</sub> compound, prepared using hydrothermal method was tested for *in vivo* imaging and was shown to be a suitable biomarker.<sup>4,5</sup> However for solid state synthesis, 0.5 mol% Cr<sup>3+</sup> doping was found to be the optimum concentration to obtain the highest LLP.<sup>6</sup> Recently, many other modified gallate spinels doped with Cr<sup>3+</sup> ions have been discovered that show similar red/NIR LLP emission. Pan *et al.* reported Cr<sup>3+</sup> doped zinc gallogermanates which showed a very long NIR afterglow.<sup>7</sup> An extensive study was conducted by Allix *et al.* on Ge and Sn substituted zinc gallates and they concluded that substitution of Ga<sup>3+</sup> by Ge<sup>4+</sup> or Sn<sup>4+</sup> in octahedral sites probably increases inversion in the spinel structure, although the substitution may play an extra role in creating more local defects and increase the delayed emission.<sup>8</sup> Lately, Cr<sup>3+</sup> doped

<sup>a</sup> Department of Physics, Goa University, Taleigao plateau, Goa 403206, India.

E-mail: krp@unigoa.ac.in; Tel: +91 0832 651 9084

<sup>b</sup> PSL Research University, Chimie ParisTech – CNRS, Institut de Recherche de Chimie Paris, 75005, Paris, France

† Electronic supplementary information (ESI) available. See DOI: 10.1039/c4cp03866e

magnesium gallate was also shown to be a good enough phosphor for *in vivo* imaging with the argument that structural inversion is an important factor governing the LLP properties.<sup>9</sup> However, the ZnGa<sub>2</sub>O<sub>4</sub> host is a much preferred material to study the LLP mechanism due to its comparatively simpler structure and well resolved Cr<sup>3+</sup> energy levels.

ZnGa<sub>2</sub>O<sub>4</sub> is known to crystallize in the normal spinel structure (cubic space group *Fd3m*) with Zn<sup>2+</sup> ions in tetrahedral coordination and Ga<sup>3+</sup> ions in octahedral coordination. However, the existence of a few percent of inversion in site occupancies of Zn and Ga is reported in the literature.<sup>3,8,10–12</sup> Among the spinel family AB<sub>2</sub>O<sub>4</sub> (with A = Zn, Mg and B = Ga, Al), MgGa<sub>2</sub>O<sub>4</sub> is by and large an inverse spinel compound with about 44% octahedral sites occupied by Mg<sup>2+</sup> ions.<sup>9,13</sup> On the other hand, ZnAl<sub>2</sub>O<sub>4</sub> is reported to be a near normal spinel structure with less than 1% cation disorder.<sup>14</sup> When these spinels are doped with Cr<sup>3+</sup> in octahedral positions and excited by UV/X-rays, they emit in the red/NIR region (around 700 nm). This emission arises due to the <sup>2</sup>E(<sup>2</sup>G) → <sup>4</sup>A<sub>2</sub>(<sup>4</sup>F) Cr<sup>3+</sup> d–d transition.<sup>3,9,15</sup>

Very recently, the LLP mechanism was investigated in detail in thermally stimulated luminescence (TSL) studies conducted on chromium doped zinc gallate demonstrating that, direct d–d excitation of Cr<sup>3+</sup> ions by visible light gives a persistent luminescence dominated by Cr<sup>3+</sup> ions possessing an antisite defect in its first cationic neighbour (referred to as the Cr<sub>N2</sub> ion).<sup>16</sup> The essential feature of the proposed mechanism is that charge separation and trapping occur with the assistance of the local electric field created by the presence of a pair of complementary antisite defects around Cr<sup>3+</sup> ions. Thus the energy is stored in the form of an electron–hole pair and does not involve a change in the valence state of the Cr<sup>3+</sup> ion. The model efficiently explains how LLP can be excited even with lower energy visible radiation.<sup>16</sup> This hypothesis was further augmented by electron paramagnetic resonance (EPR) studies carried out on chromium doped zinc gallate compounds with a varying Zn/(Ga + Cr) nominal ratio.<sup>17</sup> The defects around chromium were identified by correlating photoluminescence (PL) and EPR spectroscopy. Here again it was shown that Cr<sub>N2</sub> ion plays a key role in both LLP excitation and emission.<sup>17</sup>

To further substantiate the mechanism deduced from optical and EPR studies, X-ray absorption fine structure spectroscopy (XAFS) measurements were carried out in Cr<sup>3+</sup> doped ZnGa<sub>2</sub>O<sub>4</sub> to understand the local structures around all the cations. Moreover, the validity of the mechanism is extended by studying the local environment of Cr<sup>3+</sup> in MgGa<sub>2</sub>O<sub>4</sub>:Cr<sup>3+</sup> and ZnAl<sub>2</sub>O<sub>4</sub>:Cr<sup>3+</sup>. Based on the interference from a photoelectron wave emitted from an atom due to the absorption of an X-ray photon and a back scattered wave resulting due to its scattering from neighboring ions, XAFS provides information about immediate surroundings of the central absorbing ion. Therefore, XAFS can be used to probe structural defects around a metal ion and is an ideal technique for understanding the local structure of an atom in the lattice. It works virtually for all elements and even in cases where the concentration of absorbing ion is very low (few ppm). This makes it a versatile tool to study persistent luminescence

materials since the dopant concentration will usually be very low.<sup>18–28</sup> In this paper, we have carried out XAFS measurements at Cr K edges in chromium doped ZnGa<sub>2</sub>O<sub>4</sub>, MgGa<sub>2</sub>O<sub>4</sub> and ZnAl<sub>2</sub>O<sub>4</sub> compounds, also characterized by optical and EPR spectroscopy. Further, local structures around Zn, Ga and Cr have been studied in Cr<sup>3+</sup> doped ZnGa<sub>2</sub>O<sub>4</sub> compounds with a varying Zn/Ga nominal ratio.

## 2 Experimental

The samples were synthesized using the solid state method with their respective metal oxides ZnO (Sigma-Aldrich 99.99% pure), Ga<sub>2</sub>O<sub>3</sub> (Sigma-Aldrich 99.99% pure), MgO (Sigma-Aldrich 99.995% pure), Al<sub>2</sub>O<sub>3</sub> (SRL 99.75% pure) and CrO<sub>3</sub> (SRL 99% pure) as precursors. Weighed powders along with propan-2-ol were thoroughly mixed in an agate mortar and the dried mixture was pelletized under a 4 ton pressure in a hydraulic press. All the pellets were annealed in air at 1300 °C for 6 hours except ZnAl<sub>2</sub>O<sub>4</sub>, which was annealed at 1400 °C, and later crushed to get fine powders for further characterization. ZnGa<sub>2</sub>O<sub>4</sub> (noted ZGO) compounds were prepared in three different molar ratios – Zn/Ga = 0.5 (noted s-ZGO for stoichiometric ZGO), Zn/Ga = 0.495 (d-ZGO for 1 mol% Zn deficiency) and Zn/Ga = 0.505 (e-ZGO for 1 mol% Zn excess) with 0.5 mol% Cr introduced relative to Ga. It has to be noted that varying the nominal Zn/Ga ratio in the reactant mix does not mean that Zn or Ga atoms are in excess/deficiency in the obtained ZGO compounds. It was indeed shown that tiny quantities of ZnO/Ga<sub>2</sub>O<sub>3</sub> could either be present as very minor impurities or evaporate during the high temperature synthesis.<sup>17</sup> However, varying the nominal Zn/Ga ratio had a very definite effect on the number of point defects in d-ZGO, s-ZGO and e-ZGO compounds.<sup>3,17</sup> Therefore the letters d, s and e only reflect deficiency, stoichiometry and excess in the reactant mix without pre-supposing the stoichiometry of the actually formed ZGO compounds. To compare the effect of Cr<sup>3+</sup> doping on LLP properties in different host lattices, MgGa<sub>2</sub>O<sub>4</sub> (noted MGO) with 1 mol% Mg deficiency (noted d-MGO) and 0.5 mol% Cr doping relative to Ga, and ZnAl<sub>2</sub>O<sub>4</sub> (noted ZAO) with 1 mol% Zn deficiency (noted d-ZAO) and 0.5 mol% Cr doping relative to Al, were synthesized.

Room temperature (RT) photoluminescence (PL) excitation spectra were recorded on a Varian Cary Eclipse spectrofluorimeter in the range 190–650 nm with a xenon lamp as the excitation source. Pulsed laser excited PL was run on 8 mm-diameter pellets silver glued on the cold finger of a cryogenic system maintained at 20 K. The emitted light was collected using an optical fiber and transmitted to a Scientific Pixis 100i CCD camera cooled at –20 °C and coupled to a monochromator with 1200 grooves per mm grating. The pellets were excited at 230 nm using an optical parametric oscillator (OPO) EKSPAL NT342B. The PL emission spectra were measured with a 10 ms gate width and 26 ns gate delay. LLP measurements were carried out at RT on 180 mg samples filled into a 1 cm diameter circular sample holder. The samples were illuminated for 15 minutes

using X-rays (Mo-tube, 20 mA–50 kV) or for 30 minutes in the  ${}^4A_2 \rightarrow {}^4T_2$   $Cr^{3+}$  band using OPO. After this excitation, emission was collected using a Scientific Pixis 100 CCD camera *via* an optical fiber linked to an Acton SpectraPro 2150i spectrometer for spectral analysis. LLP emission spectra were recorded during the excitation and 5 s after the end of excitation. All the samples were bleached at 250 °C for 30 minutes and were kept in the dark prior to LLP measurements.

X-band ( $\sim 9.4$  GHz frequency) EPR spectra were recorded at room temperature on weight normalized samples using a Bruker Elexsys E500 continuous wave spectrometer. The powder spectra were simulated using the X-Sophe software tool from Bruker.

A Rigaku X-ray diffractometer was used to obtain the X-ray diffraction (XRD) patterns at RT using Cu-K $\alpha$  radiation. The spectra were recorded in the  $2\theta$  range of 20–80° in steps of 0.02° and 2° min $^{-1}$  scan speed. Rietveld refinement on the XRD patterns was carried out using FullProf software.<sup>29</sup> XAFS at RT were measured on the samples in fluorescence mode for Cr K edge and in transmission mode for Zn K and Ga K edges, at SAMBA beamline in the Soleil synchrotron facility, France. The Si (111) crystal plane was used as the monochromator. For fluorescence measurements, absorbers were prepared by mixing 50 mg compound with 100 mg boron nitride and pressing each of them into 10 mm pellets while for transmission, an appropriate amount of finely ground powder was deposited on a membrane. Fluorescence yield was collected *via* a Canberra 35 pixels SSD detector and the transmitted photons were counted using an ionization chamber with the appropriate gases. Extended X-ray absorption fine structure spectroscopy (EXAFS) fitting was carried out using Ifeffit software using the Athena and Artemis programs.<sup>30</sup> EXAFS data in the  $k$  range of 2 to 11 Å $^{-1}$  for Zn, 2 to 14 Å $^{-1}$  for Ga and 3 to 10 Å $^{-1}$  for Cr K edge were Fourier transformed, and the fitting was performed in the  $R$  range of 1 to 3.6 Å to obtain reasonable fits. Theoretical amplitude and phase information for various scattering paths were obtained using FEFF 6.01<sup>31</sup> and the Rietveld refined parameters.

### 3 Results

The photoluminescence excitation spectra measured at RT for s-ZGO, e-ZGO, d-ZGO, d-MGO and d-ZAO are presented in Fig. 1(a). The spectra consist of host band gap excitation peaking at about 245 nm for ZGO compounds, 230 nm for d-MGO and 205 nm for d-ZAO, and three broad absorption bands at around 230–270 nm, 410 nm and 560 nm belonging to the  ${}^4A_2({}^4F) \rightarrow {}^4T_1({}^4P)$ ,  ${}^4A_2({}^4F) \rightarrow {}^4T_1({}^4F)$  and  ${}^4A_2({}^4F) \rightarrow {}^4T_2({}^4F)$   $Cr^{3+}$  d–d transitions, respectively. It was previously shown that the crystal field around the  $Cr^{3+}$  ion in d-MGO is weaker than that of ZGO compounds and hence a red shift is seen in the  $Cr^{3+}$  absorption bands of d-MGO compared to those of ZGO.<sup>9</sup> In contrast, in d-ZAO, the  $Cr^{3+}$  absorption bands are shifted to shorter wavelengths compared to ZGO compounds indicating that the crystal field around  $Cr^{3+}$  ion is stronger than those of ZGO. Within the ZGO compounds, the  $Cr^{3+}$  absorption bands

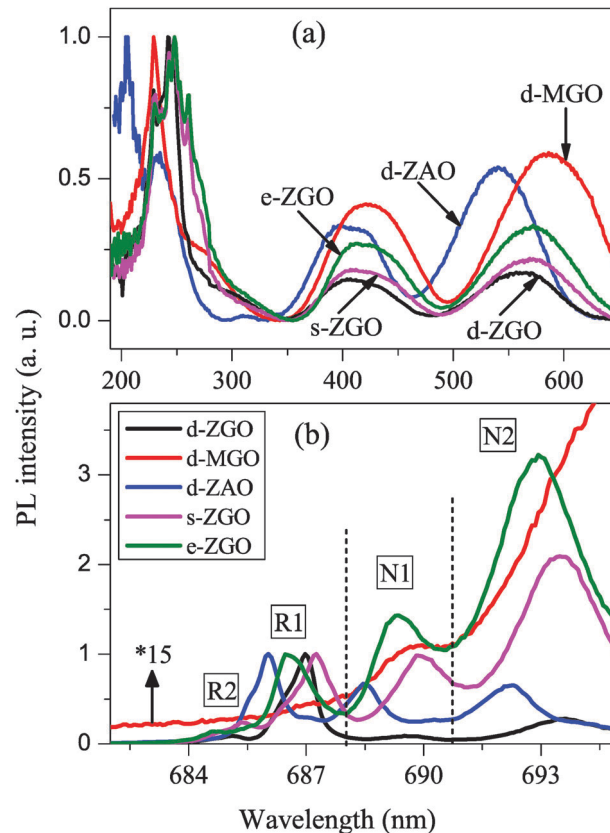


Fig. 1 (a) PL excitation spectra of  $Cr^{3+}$  doped ZGO compounds with varying Zn/Ga nominal ratio, d-MGO and d-ZAO compounds, measured at room temperature. (b) Corresponding zero-phonon PL emission spectra at 20 K and excited at 230 nm.

are seen to be gradually moving towards longer wavelengths with the increasing Zn/Ga nominal ratio (deficiency to stoichiometric to excess) revealing a decrease in the crystal field around  $Cr^{3+}$  ions.

The influence of defects around  $Cr^{3+}$  ions among different samples could also be seen in PL emission at 20 K under 230 nm excitation (Fig. 1(b)). The emission lines correspond to the typical  ${}^2E \rightarrow {}^4A_2$  transitions of  $Cr^{3+}$  either in an unperturbed environment and/or with perturbation from the nearby crystal defects. Only zero phonon lines (ZPL) are shown in Fig. 1(b). Multi phonon side bands (PSB), which occur at shorter wavelengths, are not shown here. For the sake of comparison, the spectra except for d-MGO sample are normalized to the R1 line. The d-MGO spectrum is amplified by a factor of 15 with respect to d-ZGO, for better visibility and comparison. The emission spectra can be categorized into three main ZPL regions, namely, (i) R1 and R2 region; (ii) N1 region and (iii) N2 region, separated by dotted lines in Fig. 1(b). R1 and R2 lines correspond to the  $Cr^{3+}$  ions with an unperturbed ideal environment (referred to as  $Cr_R$  centers). The distinct R1 and R2 lines are ascribed to the splitting of the  ${}^2E$  excited state of  $Cr^{3+}$  due to trigonal distortion into two levels separated by  $\sim 40$  cm $^{-1}$  in ZGO and  $\sim 7$  cm $^{-1}$  in ZAO.<sup>32,33</sup> Similarly, the N1 line (referred to as  $Cr_{N1}$ ) may correspond to either a  $Cr^{3+}-V_{Zn}$

**Table 1** Characteristics of zero-phonon emission lines (ZPL) of Cr<sup>3+</sup>-doped ZGO, ZAO and MGO compounds<sup>a</sup>

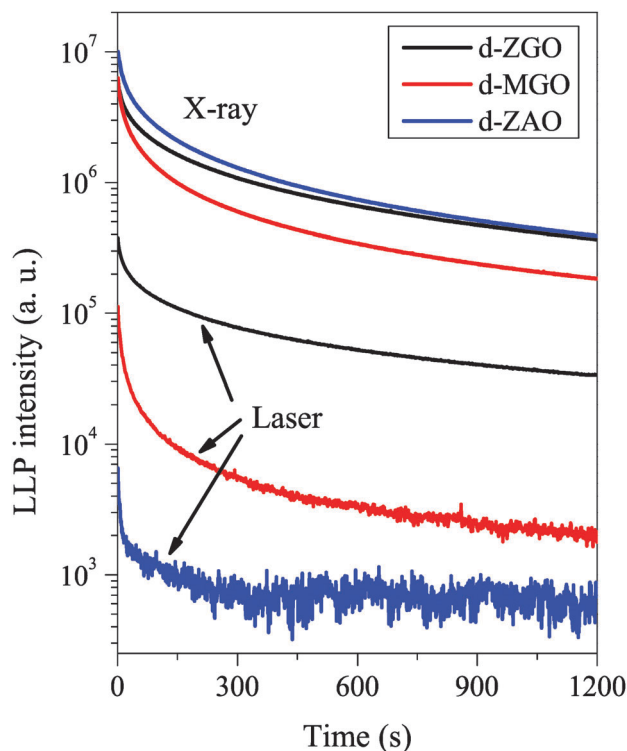
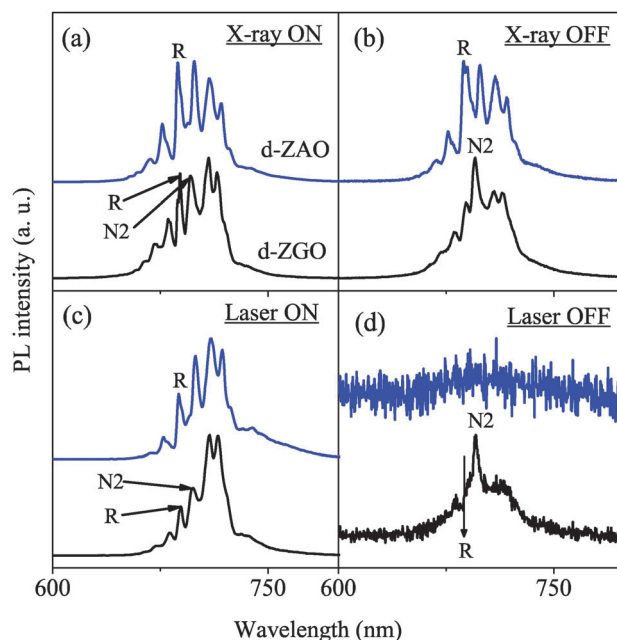
Sample	ZPL emission line (682–695 nm)			
	R1 (nm)	R2 (nm)	N1 (nm)	N2 (nm)
d-ZAO	686.0	684.2	688.5	692.2
d-ZGO	686.4	684.6	689.3	692.9
s-ZGO	686.9	685.1	689.7	693.4
e-ZGO	687.2	685.4	689.9	693.6
d-MGO	N. V.	N. V.	N. V.	N. V.

<sup>a</sup> N. V. – Not visible.

pair ( $V_{Zn}$  is a Zn vacancy)<sup>15</sup> or a Cr<sup>3+</sup>-Zn<sub>i</sub> pair (Zn<sub>i</sub> is an interstitial Zn)<sup>34</sup> or a Cr<sup>3+</sup> close to an antisite defect.<sup>17,33</sup> The N2 line is assigned to the presence of antisite defects (presumably Zn<sub>Ga</sub>) close to the Cr<sup>3+</sup> ion as first cationic neighbour (referred to as Cr<sub>N2</sub>).<sup>17,33,35,36</sup> The emission wavelengths of all these lines are reported in Table 1. As N lines are due to Cr<sup>3+</sup> being perturbed by neighboring antisite defects, their intensity (compared to R lines) increases with increasing inversion disorder. This shows that d-ZAO and d-ZGO are the less disordered materials, followed by s-ZGO and e-ZGO in the increasing order. The disorder is so high in d-MGO that emission features are difficult to interpret and the main emission line is situated at 707 nm with total of six ZPLs revealing up to six different environments for Cr<sup>3+</sup> ions.<sup>9</sup>

The persistent luminescence decay curves obtained using X-ray and laser (wavelength at the maximum of  ${}^4A_2({}^4F) \rightarrow {}^4T_2({}^4F)$  Cr<sup>3+</sup> d-d transition) excitations are presented in Fig. 2. d-MGO is known to show less LLP intensity compared to ZGO with both X-ray and laser excitations as reported earlier.<sup>9</sup> This is presumably due to excess cationic inversion which partially quenches LLP by introducing a direct recombination pathway between abundant defects.<sup>9</sup> The d-ZAO compound which is a near normal spinel, shows almost the same or slightly better LLP intensity as compared to the d-ZGO compound with X-ray excitation. However, d-ZAO shows a very feeble LLP intensity with 540 nm laser excitation, although this excitation corresponds to the maximum of the  ${}^4A_2({}^4F) \rightarrow {}^4T_2({}^4F)$  absorption band of Cr<sup>3+</sup>. On the other hand, d-ZGO shows consistently better LLP with both excitations as seen in Fig. 2. Also, this distinctive property of d-ZGO to show LLP with laser excitation renders the possibility for re-excitation of the ZGO nanoparticles inside the animal body by visible light illumination, making it a favourable candidate for the application of *in vivo* imaging.<sup>4,5</sup>

Comparisons of emission spectra recorded for d-ZGO and d-ZAO compounds during the excitation and during LLP emission (after the end of excitation) are shown in Fig. 3. Emission spectra measured during X-ray excitation (Fig. 3(a)) show intense R-lines for both the compounds, and correspond to the  ${}^2E \rightarrow {}^4A_2$  ZPL of Cr<sup>3+</sup>. This ZPL is flanked by multiphonon sidebands. The N2 line, which arises due to emission from Cr<sup>3+</sup> ions with an antisite defect in its first cationic neighbour, is clearly seen in the d-ZGO spectrum. It is difficult to identify the presence of N1 and N2 in d-ZAO because of the intense multi-PSB in the same range. However low temperature emission spectrum (Fig. 1(b)) without PSB clearly shows the

**Fig. 2** LLP decay curves of Cr<sup>3+</sup>-doped compounds after 15 minutes of X-ray irradiation and after 30 minutes of laser excitation of wavelength 560 nm for d-ZGO, 585 nm for d-MGO and 540 nm for d-ZAO samples. These wavelengths correspond to the maximum of the  ${}^4A_2({}^4F) \rightarrow {}^4T_2({}^4F)$  absorption band of Cr<sup>3+</sup>.**Fig. 3** Emission spectra measured for d-ZGO (black curves) and d-ZAO (blue curves) (a) during X-ray irradiation; (b) 5 s after the end of 15 minutes of X-ray illumination; (c) during optical laser excitation at 540 nm for d-ZAO and 560 nm for d-ZGO; (d) 5 s after the end of 30 minutes of laser excitation. Expected position of the R-line is indicated by an arrow.

presence of N1 and N2 lines. The X-ray excited LLP emission spectrum for d-ZAO shows an intense R-line (which is weakly split) whereas d-ZGO exhibits a prominent N2 line (Fig. 3(b)). This indicates that for X-ray excitation, the charge recombination is taking place mainly at undistorted  $\text{Cr}_R^{3+}$  ions ( $\text{Cr}_R$ ) in d-ZAO, while it occurs through  $\text{Cr}_{N2}$  in d-ZGO. Upon laser excitation, the emission spectra recorded while the laser is on (Fig. 3(c)) show R and N2 lines for both compounds. When the laser is switched off (LLP emission), d-ZAO shows a broad weak emission (Fig. 3(d)), whereas d-ZGO spectrum again exhibits a prominent N2 line. This indicates the crucial role of  $\text{Cr}_{N2}$  ions and antisite defects in LLP emission when excited in low energy absorption bands of  $\text{Cr}^{3+}$ .

Experimental and simulated EPR spectra of  $\text{Cr}^{3+}$  in d-ZAO, d-ZGO and d-MGO are reported in Fig. 4. For the direct spinels d-ZGO and d-ZAO, which exhibit a weak inversion disorder, the spectrum is composed of a strong line around 175 mT, a weak line around 330–350 mT and other lines at  $\sim 800$  mT in d-ZGO and  $\sim 1100$  mT in d-ZAO. These spectra were simulated with the EPR parameters of a  $\text{Cr}^{3+}$  ion in a weakly axially distorted octahedral site, in agreement with the  $C_3$  symmetry of Ga and Al sites in these compounds. The effect of antisite defects is a strain broadening of these EPR lines, which increases with magnetic field strength so that EPR lines at high magnetic field are no longer observed in s-ZGO and e-ZGO.<sup>17</sup> A zoom of transition at the low magnetic field (175 mT) shows that the line is slightly broader in d-ZGO than in d-ZAO, pointing to a slightly higher disorder in d-ZGO than in d-ZAO. The inverse

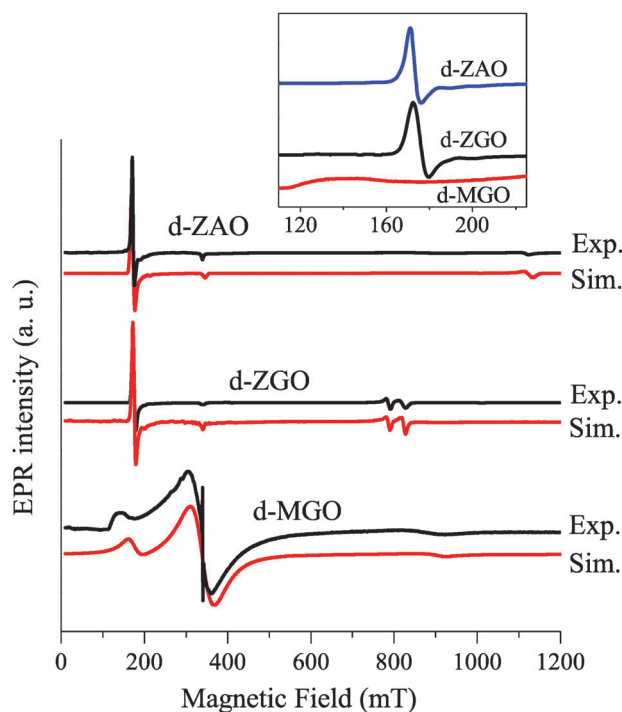


Fig. 4 X-band EPR spectra of d-ZAO, d-ZGO and d-MGO recorded at room temperature. Microwave power 2 mW; modulation depth 1 mT at 100 kHz modulation frequency. The inset shows a zoom of the low magnetic field part of the spectra.

spinel d-MGO gives a very different EPR spectrum. We still recognize broad lines at  $\sim 130$  to 150 mT (see also the inset in Fig. 4) and at  $\sim 900$  mT attributable to  $\text{Cr}^{3+}$  in octahedral sites affected by an important disorder due to abundant antisite defects. The spectrum also exhibits a broad and symmetrical line in the field range of  $\sim 300$  mT. This line was also observed in the disordered s-ZGO and e-ZGO materials.<sup>17</sup> Based on the temperature dependence of its intensity, this line was tentatively attributed to clusters of antiferromagnetically coupled  $\text{Cr}^{3+}$  ions.<sup>17</sup> The decomposition of the simulated spectrum of  $\text{Cr}^{3+}$  in d-MGO is shown in the ESI,† Fig. S1, and the simulation parameters of all compounds are reported in the ESI,† Table S1. The parameter which controls the shape of the powder EPR spectrum of  $\text{Cr}^{3+}$  in these compounds is the zero field splitting (ZFS) parameter  $D$ . It represents the splitting  $2D$  of the  $^4A_2$  ground state by the combined effect of the spin–orbit coupling and the trigonal distortion of the octahedral crystal field. d-ZAO exhibits the largest splitting ( $2D = 1.864 \text{ cm}^{-1}$ ) compared to d-MGO ( $2D = 1.270 \text{ cm}^{-1}$ ) and d-ZGO ( $2D = 1.050 \text{ cm}^{-1}$ ). This corresponds to a decreasing trigonal distortion in the sequence d-ZAO  $\gg$  d-MGO  $>$  d-ZGO, which can be compared to octahedral crystal field splitting decreasing in the sequence d-ZAO  $>$  d-ZGO  $>$  d-MGO (see Fig. 1(a)). Thus the aluminate d-ZAO has more crystal field splitting  $D$ , more trigonal distortion and less antisite disorder than gallates d-ZGO and d-MGO.

To complement optical and EPR studies, and to investigate in more detail the environment around  $\text{Cr}^{3+}$  ion in these lattices, structural studies including XRD and EXAFS measurements have been carried out. The XRD patterns of all the compounds s,d,e-ZGO, d-MGO and d-ZAO are shown in the ESI,† Fig. S2 and Rietveld refinement parameters are given in the ESI,† Table S2. XRD indicates the formation of pure cubic spinel compounds. As previously reported, a minor  $\sim 1\%$  MgO impurity in the d-MGO compound (marked + in the ESI,† Fig. S2) is identified.<sup>9</sup> A clear shift in the peak positions is observed in the  $\text{Cr}^{3+}$  doped host lattices spectra, corresponding to the variation in lattice parameters which is mostly the result of difference in the ionic sizes of cations. The lattice parameter decreases in the sequence ZGO  $>$  d-MGO  $>$  d-ZAO. Not much variation was seen among ZGO compounds; however, Rietveld refinement indicated lowering lattice constant values with increasing Zn/Ga nominal ratio. Rietveld refinement was carried out on all the XRD patterns with A site cations in tetrahedral 8a positions (site symmetry:  $T_d$ ) and B site cations in octahedral 16d positions (site symmetry:  $D_{3d}$ ).<sup>37</sup> Parameters like the lattice constant, cationic site occupancy along with scale factor, background and instrumental parameters were varied while fitting. The fits to the experimental patterns along with residues are shown in the ESI,† Fig. S2. The cationic occupancy could not be varied for ZGO compounds since  $\text{Zn}^{2+}$  and  $\text{Ga}^{3+}$  ions are isoelectronic having similar X-ray scattering powers for the Cu-K $\alpha$  radiations. As reported earlier, the d-MGO compound shows 45.2(3)% cationic site inversion confirming the near inverse spinel structure.<sup>9</sup> The site occupancy was also varied for the d-ZAO compound and yielded no inversion in the lattice, hinting towards its normal spinel crystal structure.

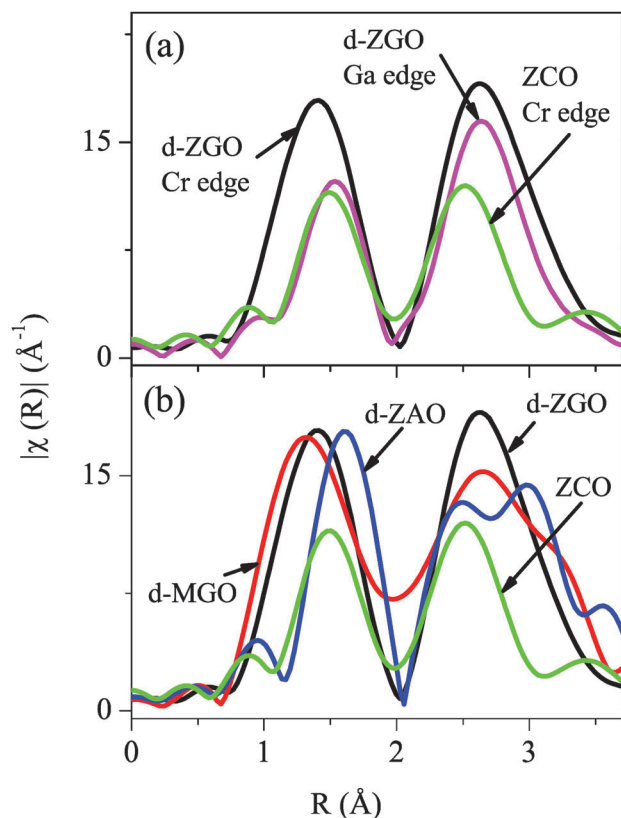


Fig. 5 Fourier transform magnitude of EXAFS pattern in the  $k$  range 3 to  $10 \text{ \AA}^{-1}$  (a) of Cr K edge and Ga K edge for d-ZGO and ZCO; (b) of Cr K edge for d-ZGO, d-MGO, d-ZAO and ZCO.

EXAFS measurements were carried out on the  $\text{Cr}^{3+}$  doped ZGO, d-MGO and d-ZAO compounds, along with the  $\text{ZnCr}_2\text{O}_4$  (noted ZCO) compound, which was used as a reference for the octahedral  $\text{Cr}^{3+}$  environment. Magnitudes of the Fourier transform (FT) of Cr K and Ga K edge EXAFS in d-ZGO are presented in Fig. 5(a) in comparison with the Cr K edge spectrum of ZCO. The Cr K EXAFS spectra in all three ZGO compounds are largely similar and hence the individual spectra are not presented here. It can be seen that the first peak corresponding to Cr–O correlation in the d-ZGO Cr edge appears at a lower  $R$  value compared to the first peak in both the d-ZGO Ga edge and the ZCO Cr edge, which implies that the average Cr–O distance in d-ZGO is less than the Ga–O distance in the same compound or the Cr–O distance in ZCO. This anomaly gains more importance because unlike the first peak, the second intense peak observed around  $2.7 \text{ \AA}$  in d-ZGO Cr edge spectrum is almost at the same position as that in the d-ZGO Ga edge spectrum. Also, an asymmetrical peak broadening of the first peak is observed in the d-ZGO Cr edge spectrum revealing a distribution of Cr–O bond distances, especially towards the shorter distances. These observations indicate that the local octahedral environment around the  $\text{Cr}^{3+}$  ion is largely distorted compared to that of the  $\text{Ga}^{3+}$  environment in ZGO or the ideal octahedral  $\text{Cr}^{3+}$  environment in ZCO. The FT magnitudes of  $k$  weighted EXAFS spectra of  $\text{Cr}^{3+}$  doped host lattices are presented in Fig. 5(b). A comparison of the FT magnitudes in the host lattice compounds

with that of ZCO shows Cr–O distances in d-ZGO and d-MGO to be shorter than that in ZCO. Again the peaks are asymmetrically broadened, indicating a distribution in the Cr–O bond distances. However in d-ZAO, the Cr–O distance is larger than that in ZCO and no broadening is seen in the peak, indicating a smaller distribution of the Cr–O distances.

Experimentally obtained EXAFS spectra were fit using Iffeffit software for all the compounds to obtain bond distances ( $R$ ) and mean-square disorders ( $\sigma^2$ ) for each path. The raw spectra were background corrected and energy calibrated using Athena and then fitted using Artemis. Atomic coordinates and lattice parameters obtained for each compound using the Rietveld refinement were used as inputs to generate a FEFF input file, with Cr or Zn or Ga as the core for the corresponding Cr or Zn or Ga K edge spectra. The photoelectron scattering paths were then calculated and the experimental data was fitted up to  $3.6 \text{ \AA}$  in the  $R$ -space to obtain  $R$  and  $\sigma^2$  for each scattering path. Goodness of the fit, expressed by the  $R$  factor, was less than 0.03 in all the fits. The Cr K EXAFS in the d-ZGO compound could only be fitted using the third cumulant parameter ( $C_3$ ) which indicates an asymmetrical distribution of Cr–O bond distances. All other attempts to fit the spectra resulted in negative (unphysical) values of  $\sigma^2$ . This deviation away from a normal distribution of Cr–O bond distances can be explained to be due to the disorder around the  $\text{Cr}^{3+}$  ion, resulting in an asymmetric distribution of bond distances. An example of fit to EXAFS data in the back transformed  $k$  space is presented in Fig. 6 for d-ZGO. Other fits for the Zn K edge and Ga K edge EXAFS patterns of d-ZGO are shown in the ESI,<sup>†</sup> Fig. S3. All the fitting parameters are given in the ESI,<sup>†</sup> Table S3 for Cr K edge EXAFS and Table S4 for Zn K and Ga K EXAFS.

Unlike ZGO compounds, Cr K EXAFS in d-MGO could be fitted starting with two structural models based on the normal spinel structure with Mg occupying all tetrahedral sites and Ga occupying octahedral sites, and the inverse spinel structure wherein all the Mg ions occupied octahedral sites and half of

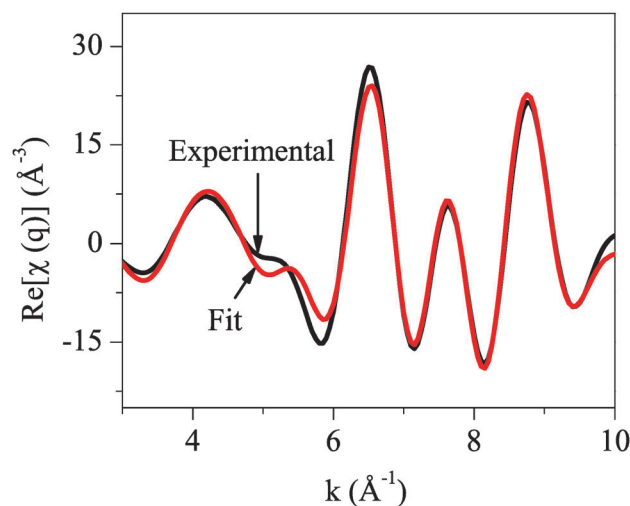


Fig. 6 Experimentally obtained Cr K edge EXAFS pattern for d-ZGO along with fit in  $q$  space in the  $k$  range 3 to  $10 \text{ \AA}^{-1}$ .

the Ga ions occupied the tetrahedral sites. The phase fraction of each model was taken as a fitting parameter. The inversion around  $\text{Cr}^{3+}$  for d-MGO was found to be 44(5)% which is consistent with the value 45.2(3)% obtained using Rietveld refinement. In the case of d-ZAO, the best fit was obtained using the normal spinel model, indicating the presence of very little or no inversion around the  $\text{Cr}^{3+}$  ion.

## 4 Discussion

This work contributes to our effort to explain an unexpected property of  $\text{Cr}^{3+}$ -doped ZGO, which is the possibility of activating LLP using visible light. Owing to the leading role of  $\text{Cr}^{3+}$  ions in this property, we examined the perturbation in the  $\text{Cr}^{3+}$  environment by structural defects, mainly antisite defects due to inversion disorder. By combining PL, TSL and EPR analyses, we recently proposed a mechanism whereby LLP excitation and emission are likely due to a particular type of [ $\text{Cr}^{3+}$ -defect] cluster ( $\text{Cr}_{\text{N}_2}$ ), namely a  $\text{Cr}^{3+}$  ion with two neighboring antisite defects of opposite charge (a  $\text{Zn}'_{\text{Ga}}$  defect at short distance and a  $\text{Ga}^{\circ}_{\text{Zn}}$  defect at longer distance).<sup>16,17</sup> In this mechanism, it was proposed that the electric field created by the two neighboring defects of opposite charge triggers the formation of electron-hole pairs from the excited  ${}^4\text{T}_2$  chromium state (or other states of higher energy), the hole and the electron being the next trapped at  $\text{Zn}'_{\text{Ga}}$  site and  $\text{Ga}^{\circ}_{\text{Zn}}$  site of the lattice, respectively. The present structural study provides a deeper insight into this still speculative model. The importance of antisite defects is now clearly supported by the correlation between the amount of inversion disorder and the excitation of LLP by visible light. ZGO is characterized by a few percent of inversion ( $\sim 3\%$ ),<sup>8</sup> which appears to be a good compromise for this optical property. In contrast, d-ZAO exhibits no measurable inversion and no strain broadening of the EPR, PL and XAFS spectra, and clearly shows no considerable visible light excited LLP, although it still exhibits a strong X-ray excited LLP (Fig. 2). Indeed TSL studies of this compound clearly show the lack of TSL peaks arising due to antisite defects (occurring at 370 K).<sup>38</sup> d-MGO shows a high level of inversion disorder ( $\sim 45\%$ ) which manifests itself by strong strain broadening effects in the EPR, PL and XAFS spectra. This compound presents a less efficient visible light excited LLP than d-ZGO, presumably due to a parasitic direct recombination of trapped charges (Fig. 2). Antisite defects are thus crucial to allow the excitation, charge trapping and emission of the LLP, when excited by visible light. The effect of these cationic defects and more generally, of the nature of cations on the  $\text{Cr}^{3+}$  environment, is shown in Fig. 7 which correlates interatomic distances, lattice parameters and crystal field energies. It appears that Cr–Zn (or Cr–Mg) distances (open squares in Fig. 7(a)) and Cr–Ga (or Cr–Al) distances (full squares in Fig. 7(a)) are entirely determined by lattice parameters (see also the ESI,<sup>†</sup> Tables S3 and S4). The presence of defects does not affect this correlation as shown by the fact that d-ZGO, s-ZGO and e-ZGO have almost the same lattice parameters and the same Cr–Ga distances of 2.95 Å.

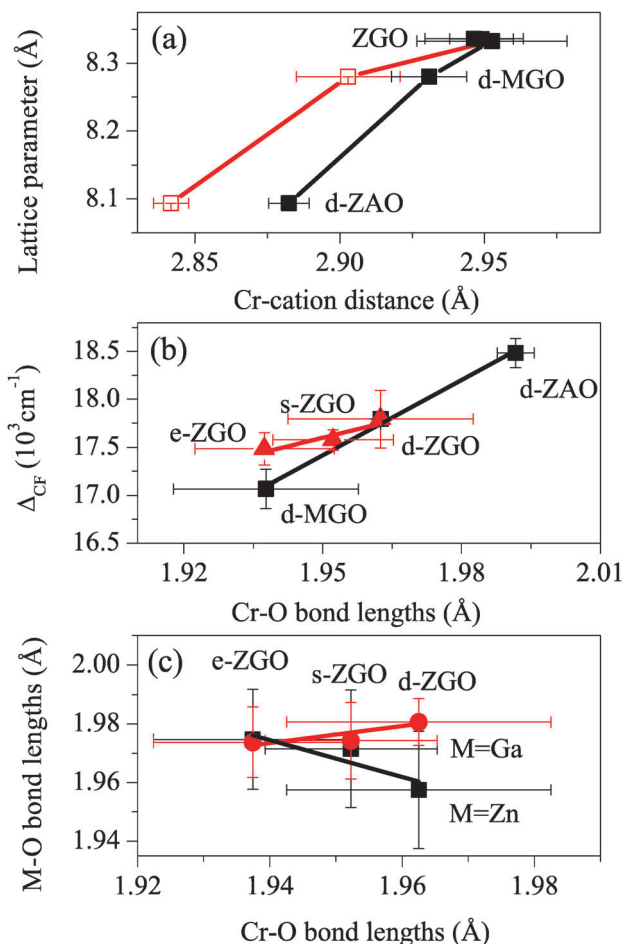


Fig. 7 (a) Rietveld refined lattice parameter values plotted versus Cr–first cationic neighbour distances obtained by EXAFS fitting. Filled black squares represent Cr–trivalent ion distances and open red squares represent Cr–divalent ion distances. The three ZGO compounds (d-ZGO, s-ZGO and e-ZGO) have almost same values and they are seen to be overlapping. (b) Crystal field energy  $\Delta_{\text{CF}}$  calculated from  ${}^4\text{A}_2 \rightarrow {}^4\text{T}_2$   $\text{Cr}^{3+}$  absorption band in RT PL spectra versus Cr–O bond lengths obtained from EXAFS fitting. (c) Metal–oxygen bond lengths (with M = Ga, Zn) plotted versus Cr–O bond lengths obtained from EXAFS fitting for ZGO compounds. Filled squares represent Zn–O bond lengths and filled circles represent Ga–O bond lengths.

Contrary to Cr–cation distances, there is no correlation between Cr–O bond lengths and lattice parameters (see the ESI,<sup>†</sup> Table S3). However a linear correlation is clearly observed in Fig. 7(b) between the Cr–O bond length and the crystal field energy  $\Delta_{\text{CF}}$  deduced from the  ${}^4\text{A}_2 \rightarrow {}^4\text{T}_2$  absorption band of  $\text{Cr}^{3+}$ , which occurs at energy  $h\nu = \Delta_{\text{CF}}$ . This correlation and the lack of correlation with lattice parameter show that  $\text{Cr}^{3+}$  imposes its first shell environment. This can be understood by considering the relation between the strength of the Cr–O bond and the crystal field splitting energy as shown in Fig. 8. In a purely ionic model, and ignoring for the moment the electron repulsion, the electronic configuration of  $\text{Cr}^{3+}$  in an octahedral environment is  $t_2^3e^0$  with a crystal field splitting  $\Delta_{\text{CF}}$  between  $t_2$  and  $e$  levels. Oxygen 2p orbitals contribute to the top of the valence band (L in Fig. 8). The  $t_2$  and  $e$  metal orbitals are separated from the

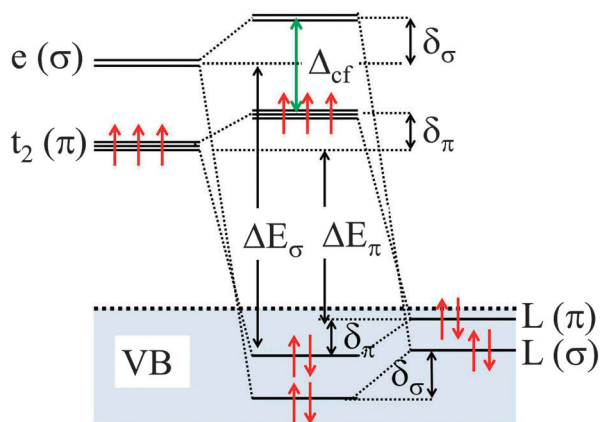


Fig. 8 Energy level scheme representing the effect of  $\sigma$  and  $\pi$  contributions to the Cr–O bond.

valence band by energies of the order of  $\Delta E_\pi$  and  $\Delta E_\sigma$ , respectively. The  $\pi$  and  $\sigma$  covalent characters of the Cr–O bond are described by non-zero transfer integrals  $\beta_\pi = \langle t_2 | H | L(\pi) \rangle$  and  $\beta_\sigma = \langle e | H | L(\sigma) \rangle$  between metal 3d and oxygen 2p orbitals, where  $H$  is the Hamiltonian operator and  $L(\pi)$  and  $L(\sigma)$  are the symmetry adapted linear combinations of oxygen orbitals with  $\pi$  and  $\sigma$  character, respectively. These transfer integrals are proportional to the metal–ligand overlap. A strengthening of the covalent bonding (decrease of the Cr–O bond length) will manifest itself by a shift of  $\sim \delta$  to low energy for  $L$  orbitals (bonding character) and a shift of  $\sim \delta$  to high energy for metal orbitals (antibonding character). An increase of the  $\pi$  character of the Cr–O bond will thus decrease the crystal field splitting  $\Delta_{cf}$  by an amount  $\delta_\pi \approx 2\beta_\pi^2/\delta E_\pi$ . Alternatively, an increase of the  $\sigma$  character of the bond will increase  $\Delta_{cf}$  by an amount  $\delta_\sigma \approx 2\beta_\sigma^2/\delta E_\sigma$  (Fig. 8). Within this scheme, the decrease of the Cr–O bond length observed in the sequence  $d_{Cr-O}(\text{d-ZAO}) > d_{Cr-O}(\text{d-ZGO}) > d_{Cr-O}(\text{d-MGO})$  (Fig. 7(b)) clearly corresponds to a decrease of  $\Delta_{cf}$ , which points to an increase of the  $\pi$  contribution to the Cr–O bond along this series. Alternatively, an increase of the  $\sigma$  contribution to the Cr–O bond would produce the opposite correlation, *i.e.* an increase of  $\Delta_{cf}$  associated with a decrease of the Cr–O bond length.

The same type of correlation, with a smaller slope, was also observed by varying the defect concentration in ZGO (Fig. 7(b)). As reported before, the concentration of defects around  $\text{Cr}^{3+}$  is minimum in d-ZGO and increases in the sequence d-ZGO < s-ZGO < e-ZGO.<sup>3,17</sup> The fact that the slope is smaller upon varying the defect concentration (full triangles in Fig. 7(b)) than upon varying the  $\text{A}^{2+}$  and  $\text{B}^{3+}$  cations (full squares in Fig. 7(b)) can be explained by symmetry effects. In the spinel series  $\text{AB}_2\text{O}_4$  ( $\text{A} = \text{Mg, Zn}$  and  $\text{B} = \text{Al, Ga}$ ), the symmetry of the unperturbed  $\text{Cr}^{3+}$  site is trigonal, which introduces no mixing between  $t_2(\pi)$  orbitals and  $e(\sigma)$  orbitals. An antisite defect in the first neighbour position of  $\text{Cr}^{3+}$ , and located outside the  $C_3$  axis, decreases the site symmetry which becomes non-axial.<sup>17</sup> This introduces a mixing between  $t_2$  and  $e$  orbitals, so that  $t_2$  orbitals take a small  $\sigma$  character while  $e$  orbitals take a small  $\pi$  character. As  $\sigma$  bonds are stronger than  $\pi$  bonds, this increasing  $\sigma$ – $\pi$  mixing

upon increasing the defect concentration shortens the Cr–O bond length. However, both  $t_2$  and  $e$  orbital sets are now shifted to a high energy, so that the increase of  $\Delta_{cf}$  is smaller than that for a pure axial symmetry, explaining the smaller slope in the curve  $\Delta_{cf} = f(d_{Cr-O})$  in the ZGO series. Introducing the electron repulsion between the three  $t_2$  electrons does not modify this scheme. The  ${}^2\text{E}$  state (emitting level) and the  ${}^4\text{A}_2$  state (ground state level) both correspond to the configuration  $t_2^3$  with total spins of  $S = 1/2$  and  $S = 3/2$ , respectively. The effect of the crystal field variation is much smaller for the  ${}^2\text{E}$ – ${}^4\text{A}_2$  splitting than for the  ${}^4\text{T}_2$ – ${}^4\text{A}_2$  splitting, but varies with the same trend.<sup>39</sup> This effect thus explains why lower the symmetry of the  $\text{Cr}^{3+}$  site, smaller the Cr–O bond length, and lower the energy of the  ${}^2\text{E}$ – ${}^4\text{A}_2$  emission of  $\text{Cr}^{3+}$ . This confirms the correlation previously proposed between the decreasing symmetry of the [ $\text{Cr}^{3+}$ -defect] clusters determined by EPR ( $\text{Cr}_R > \text{Cr}_{N1} > \text{Cr}_{N2}$ ) and the decreasing photon energy of the  ${}^2\text{E}$ – ${}^4\text{A}_2$  emission line.<sup>17</sup> Clusters with the lowest symmetry give the N2 emission line at the lowest photon energy, while clusters with a weaker non-axial distortion give the N1 line at higher photon energy, which are still at a lower photon energy than the R1 line of unperturbed  $\text{Cr}^{3+}$  ions in the axial symmetry.

From this EXAFS study, it is also possible to gain information about the nature of the dominant defects in the ZGO series. It has been previously shown that the less disordered ZGO material is d-ZGO, where the zinc deficiency in the starting composition compensates for the Ga loss during the high temperature synthesis.<sup>17</sup> Increasing the Zn content in the synthesis increases the defect concentration (e-ZGO > s-ZGO > d-ZGO) as shown by the increasing intensity of N1 and N2 emission lines, presumably in the form of an excess of antisite defects  $\text{Zn}'_{\text{Ga}}$ .<sup>17</sup> This hypothesis is now reinforced by the correlation between the M–O bond length ( $\text{M} = \text{Ga, Zn}$ ) and the Cr–O bond length (Fig. 7(c)). It is found that increasing the defect concentration results in an increase in the Zn–O bond length and a decrease in the Ga–O bond length (see the ESI,† Table S4). The Zn–O bond length is nearly equal to the Ga–O bond length at the highest defect concentration (e-ZGO). This behaviour can be explained by the fact that increasing the number of  $\text{Zn}^{2+}$  in  $\text{Ga}^{3+}$  sites ( $\text{Zn}_{\text{Ga}}$  antisite defects) has two effects: (i) as shown before, it lowers the symmetry of the  $\text{Cr}^{3+}$  site, which reduces the Cr–O bond length and shifts the  ${}^2\text{E}$ – ${}^4\text{A}_2$  emission to a lower energy, and (ii) it introduces more Zn–O bonds with the same length as Ga–O bonds into the lattice, which shifts the average Zn–O bond length towards that of Ga–O as observed in Fig. 7(c). The compensation for the excess of negative charge induced by  $\text{Zn}'_{\text{Ga}}$  antisite defects should be ensured by the other antisite defect  $\text{Ga}'_{\text{Zn}}$  and/or by oxygen vacancies  $\text{V}_\text{O}^\circ$ . In the case of compensation by the  $\text{Ga}'_{\text{Zn}}$  antisite defect, we expect a shortening of the Ga–O bond upon increasing the defect concentration. As there are two Ga for one Zn in the lattice, the ratio  $\text{Ga}'_{\text{Zn}}/\text{Ga}^\times_{\text{Ga}}$  should be two times smaller than the ratio  $\text{Zn}'_{\text{Ga}}/\text{Zn}^\times_{\text{Zn}}$ , where  $\text{Ga}^\times_{\text{Ga}}$  and  $\text{Zn}^\times_{\text{Zn}}$  represent Ga and Zn in their normal site. We thus expect a ratio  $R = -2$  between the slopes of the Zn–O and Ga–O variations, which is close to the experimental value of  $R \approx -2.17$  deduced from

Fig. 7(c). Thus the variations of Cr–O bond length with Zn–O and Ga–O bond lengths can be accounted for by  $Zn_{Ga}$  and  $Ga_{Zn}$  antisite defects present in the lattice. EPR spectroscopy previously indicated that the N2 emission line of LLP in ZGO might be due to a  $Cr^{3+}$  ion with a  $Zn'_{Ga}$  antisite defect in its first neighbour position (at 0.295 nm) and a  $Ga^{\circ}_{Zn}$  antisite defect at slightly larger distances.<sup>17</sup> This model is now supported by the present EXAFS study. It can also explain the origin of the considerable improvement of LLP in the gallogermanate series  $Zn_{1+x}Ga_{2-2x}Ge_xO_4$ .<sup>8</sup> In these compounds, two  $Ga^{3+}$  ions are replaced by one  $Ge^{4+}$  ion and one  $Zn^{2+}$  ion. Thus, increasing the value of  $x$  should increase the number of  $Cr^{3+}$  ions close to a negatively charged  $Zn'_{Ga}$  and a positively charged  $Ge^{\circ}_{Ga}$  defect. This defect configuration is determined in our model for the visible light induced LLP mechanism.<sup>16,17</sup>

## 5 Conclusions

The role of antisite defects in the persistent luminescence induced by visible light excitation in  $Cr^{3+}$ -doped  $AB_2O_4$  spinels (A = Zn, Mg; B = Ga, Al) was investigated by a combined optical, EPR, XRD and EXAFS study. The main conclusions are the following. (i) Visible light excitation of persistent luminescence necessitates a small degree of inversion disorder, with the optimal level corresponding to that in d-ZGO. (ii) Increasing the defect concentration decreases the Cr–O bond length and the crystal field energy, attributed to an increasing  $\pi$  bond contribution to the Cr–O interaction. (iii) Defects responsible for this Cr–O bond variation in ZGO are likely to be  $Zn'_{Ga}$  and  $Ga^{\circ}_{Zn}$  antisite defects. It can be concluded that a doping strategy which can control the amount of antisite defects should allow the optimization of the intensity and length of the persistent luminescence in  $AB_2O_4 \cdot Cr^{3+}$  spinels.

## Acknowledgements

Authors acknowledge the SAMBA beamline, Soleil synchrotron facility, for providing the beamtime. Ms Stéphanie Belin, beamline scientist, is gratefully thanked for the experimental support. Financial support from the Indo-French Centre for the Promotion of Advanced Research (IFCPAR)/ Centre Franco-Indien Pour la Recherche Avancée (CEFIPRA) is acknowledged.

## References

- S. W. S. McKeever, *Thermoluminescence of Solids, Cambridge Solid State Science Series*, Cambridge University Press, Cambridge, UK, 1985.
- Q. le Masne de Chermont, C. Chanéac, J. Seguin, F. Pellé, S. Maitrejean, J.-P. Jolivet, D. Gourier, M. Bessodes and D. Scherman, *Proc. Natl. Acad. Sci. U. S. A.*, 2007, **104**(22), 9266–9271.
- A. Bessière, S. Jacquart, K. Priolkar, A. Lecointre, B. Viana and D. Gourier, *Opt. Express*, 2011, **19**, 10131–10137.
- T. Maldiney, C. Richard, D. Scherman, D. Gourier, B. Viana and A. Bessière, *Nanoparticules à luminescence persistante excitable in situ pour imagerie optique in vivo, imagerie multimodale optique-IRM in vivo et la théranostique*, Pat., PCT/EP2013/051727, 2013.
- T. Maldiney, A. Bessière, J. Seguin, E. Teston, S. K. Sharma, B. Viana, A. J. J. Bos, P. Dorenbos, M. Bessodes, D. Gourier, D. Scherman and C. Richard, *Nat. Mater.*, 2014, **13**, 418–426.
- S. K. Sharma, A. Bessière, N. Basavaraju, K. R. Priolkar, L. Binet, B. Viana and D. Gourier, *J. Lumin.*, 2014, **155**, 251–256.
- Z. Pan, Y.-Y. Lu and F. Liu, *Nat. Mater.*, 2011, **11**, 58–63.
- M. Allix, S. Chenu, E. Ve, T. Poumeyrol, E. A. Kouadri-boudjelthia, S. Alahrache, F. Porcher and D. Massiot, *Chem. Mater.*, 2013, **25**, 1600–1606.
- N. Basavaraju, S. Sharma, A. Bessière, B. Viana, D. Gourier and K. R. Priolkar, *J. Phys. D: Appl. Phys.*, 2013, **46**, 375401.
- I.-K. Jeong, H. L. Park and S.-i. Mho, *Solid State Commun.*, 1998, **105**, 179–183.
- G. Anoop, K. M. Krishna and M. K. Jayaraj, *Appl. Phys. A: Mater. Sci. Process.*, 2008, **90**, 711–715.
- L. Chen, Y. Liu, Z. Lu and K. Huang, *Mater. Chem. Phys.*, 2006, **97**, 247–251.
- R. L. Millard, R. C. Peterson and I. P. Swainson, *Phys. Chem. Miner.*, 2000, **27**, 179–193.
- N. Kashii, H. Maekawa and Y. Hinatsu, *J. Am. Ceram. Soc.*, 1999, **82**(7), 1844–1848.
- W. Nie, F. M. Michel-Calendini, C. Linarès, G. Boulon and C. Daul, *J. Lumin.*, 1990, **46**, 177–190.
- A. Bessière, S. K. Sharma, N. Basavaraju, K. R. Priolkar, L. Binet, B. Viana, A. J. J. Bos, T. Maldiney, C. Richard, D. Scherman and D. Gourier, *Chem. Mater.*, 2014, **26**, 1365–1373.
- D. Gourier, A. Bessière, S. K. Sharma, L. Binet, B. Viana, N. Basavaraju and K. R. Priolkar, *J. Phys. Chem. Solids*, 2014, **75**, 826–837.
- A. Bessière, A. Lecointre, K. R. Priolkar and D. Gourier, *J. Mater. Chem.*, 2012, **22**, 19039–19046.
- A. Lecointre, A. Bessière, K. R. Priolkar, D. Gourier, G. Wallez and B. Viana, *Mater. Res. Bull.*, 2013, **48**, 1898–1905.
- T. Aitasalo, J. Hassinen, J. Hölsä, T. Laamanen, M. Lastusaari, M. Malkamäki, J. Niittykoski and P. Novák, *J. Rare Earths*, 2009, **27**, 529–538.
- H. Okura, T. Murakawa, Y. Miyamoto, T. Honma and K. Ohmi, *Jpn. J. Appl. Phys.*, 2012, **51**, 062602.
- Z. Qi, C. Shi, W. Zhang, W. Zhang and T. Hu, *Appl. Phys. Lett.*, 2002, **81**, 2857–2859.
- L. C. V. Rodrigues, H. F. Brito, J. Hölsä, R. Stefani, M. C. F. C. Felinto, M. Lastusaari, T. Laamanen and L. A. O. Nunes, *J. Phys. Chem. C*, 2012, **116**, 11232–11240.
- K.-S. Sohn, B. Cho, H. D. Park, Y. G. Choi and K. H. Kim, *J. Eur. Ceram. Soc.*, 2000, **20**, 1043–1051.
- T. Takeda, R.-J. Xie, N. Hirotsaki, Y. Matsushita and T. Honma, *J. Solid State Chem.*, 2012, **194**, 71–75.
- K. Korthout, K. Van den Eeckhout, J. Botterman, S. Nikitenko, D. Poelman and P. F. Smet, *Phys. Rev. B: Condens. Matter Mater. Phys.*, 2011, **84**, 085140.

- 27 J. Hölsä, T. Laamanen, M. Lastusaari, M. Malkamäki, E. Welter and D. A. Zajac, *Spectrochim. Acta, Part B*, 2010, **65**, 301–305.
- 28 P. Ghigna, S. Pin, C. Ronda, A. Speghini, F. Piccinelli and M. Bettinelli, *Opt. Mater.*, 2011, **34**, 19–22.
- 29 J. Rodriguez-Carvajal, *Physica B*, 1993, **192**, 55–69.
- 30 B. Ravel and M. Newville, *J. Synchrotron Radiat.*, 2005, **12**, 537–541.
- 31 S. I. Zabinsky, J. J. Rehr, A. Ankudinov, R. C. Albers and M. J. Eller, *Phys. Rev. B: Condens. Matter Mater. Phys.*, 1995, **52**, 2995–3009.
- 32 W. Mikenda and A. Preisinger, *J. Lumin.*, 1981, **26**, 53–66.
- 33 W. Mikenda, *J. Lumin.*, 1981, **26**, 85–98.
- 34 W. Zhang, J. Zhang, Z. Chen, T. Wang and S. Zheng, *J. Lumin.*, 2010, **130**, 1738–1743.
- 35 W. Mikenda and A. Preisinger, *J. Lumin.*, 1981, **26**, 67–83.
- 36 J. Derkosh and W. Mikenda, *J. Lumin.*, 1983, **28**, 431–441.
- 37 *International Tables for Crystallographic Volume A: Space-group symmetry*, ed. T. Hahn, Springer, The Netherlands, 2005.
- 38 S. K. Sharma, D. Gourier, B. Viana, T. Maldiney, E. Teston, D. Scherman and C. Richard, *Opt. Mater.*, 2014, **155**, 251–256.
- 39 Y. Tanabe and S. Sugano, *J. Phys. Soc. Jpn.*, 1954, **9**, 766–779.